Supplementary Information for

Dynamic rupture initiation and propagation in a fluid-injection laboratory setup with diagnostics across multiple temporal scales

Marcello Gori[a,1], **Vito Rubino**[b], **Ares J. Rosakis**[b], **Nadia Lapusta**[c,d]

[1]Corresponding Author: Marcello Gori.
E-mail: marcello.gori00@gmail.com

This PDF file includes:

Supplementary text
Figs. S1 to S4
Table S1
SI References

Supporting Information Text

On the full set of stress measurements obtained with the strain gauges. The stress tensor components are reported in Figures S2 and S3 for the case of rapid and slow pressure ramp up, respectively, and they are obtained as detailed in Strain Acquisition System. The shear σ_{12} (yellow), fault-normal σ_{22} (green) and fault-parallel σ_{11} (cyan) stresses are plotted over three temporal scales, ranging from minutes on the left (a, d, and g), to milliseconds in the center (b, e, and h) and microseconds on the right (c, f, and i). The solid, brighter lines correspond to the strain gauge positioned in proximity of the injection site just below the interface (denoted SG-0 in Figs. 2 and S1); and the dashed, darker lines correspond to the strain gauge positioned 20 mm away from SG-0 in the positive x_1-direction (SG-20 in Figs. 2 and S1).

As before, $t = 0$ denotes the initiation of the dynamic rupture. The vertical far-field load (Fig. 2, yellow arrows) is applied quasi-statically in displacement-control mode at a constant rate of strain of 6.7×10^{-5} s^{-1}. Upon reaching the final level of 15 MPa, the system switches to load-control mode, keeps the load constant, and the strain rates drastically diminish. At this point, the strain acquisition system is zeroed and the strain variations with respect to this initial condition are recorded. Thus, all strain (and stress) readings represent changes with respect to this initial condition. Significantly, under constant strain, the polymeric material undergoes slow viscoelastic relaxation. As a consequence, to keep the applied load constant, the loading frame adds small compressive displacement increments, which are recorded by the strain gauges as compressive vertical strains and, due to the Poisson's effect, tensile strains in the horizontal direction. The strain gauges measure these strains in a reference system aligned with the fault, in the x_1, x_2-direction. Hence, the accumulation of the strain signals over several minutes prior to the initiation of the dynamic rupture embeds the contribution of the viscoelastic relaxation of the polymer, and as a result the increase in stress is a potential artifact (Fig. 7a and c; Figs. S2 and S3, a, d, and g). During the quasi-static loading phase, we focus on stress changes from the viscous-flow-induced trend, and on relative variations between different locations. When the signals of the two measurements stations deviate from each other, their difference is proportional to the different amount of slip those locations experience. Over shorter timescales, during the dynamic phase, the viscoelastic material behavior mainly results in increasing in the effective elastic moduli (1–3), which we account for, as explained in Materials and Methods. The stress behavior at the locations SG-0 and SG-20 is influenced by the 2D nature of the interface (Fig. S1b). In particular, as the pressurized fluid is delivered to the interface, heterogeneous pore pressure and slip profiles arise, where patches at higher pore-pressure tend to accumulate more slip. The shear stress released at a patch through slipping is redistributed to the surrounding patches, which, in turn, experience more or less slip, depending on their local frictional strength. Locked patches, close to the slipping ones, experience shear and normal stress accumulation, while weaker patches slip more easily and accumulate less (or release) shear stress.

For the rapid pore-pressure ramp-up scenario, in the accelerated-slip phase few hundreds of milliseconds prior to the triggering of the dynamic rupture (Fig. S2b, e, and h), the shear stress σ_{12} at SG-0 (Fig. S2b, bright yellow line) and the fault-normal stress σ_{22} (Fig. S2e, bright green line) clearly evolve, both testifying that the patch around SG-0 is undergoing slip. The positive fault-parallel stress variation σ_{11} (Fig. S2h, bright cyan line) indicates that the accelerated slip is inducing a tensile lobe through SG-0 (4, 5). This suggests that the accelerated slip is nucleating somewhere in the positive x_1-direction with respect to SG-0, and its leftward tip (Fig. 2a) swipes across the SG-0 station as it propagates in the negative x_1-direction. The rightward tip during the slip-accelerated phase does not reach the SG-20 location, which does not measure any stress signal.

After the dynamic rupture initiates (Fig. S2c, f, and i), the anti-symmetric rupture pattern (4, 5) results in nearly constant levels of normal stress σ_{22} (Fig. S2f, bright green line.) The fault-parallel stress σ_{11} is characterized by a small positive signal at SG-0 and a more pronounced negative signal at SG-20 (Fig. S2i), corresponding to tensional and compressional lobes in the fault-parallel direction, associated with with the rupture initiating in the positive x_1-direction.

The slow pore-pressure ramp-up scenario exhibits a substantially different behavior compared to the rapid ramp-up one discussed above. During the accelerated-slip phase few tens of milliseconds prior to the triggering of the dynamic rupture (Fig. S3b, e, and h), the shear stress increase σ_{12} at SG-0 (Fig. S3b, bright yellow line) more pronounced than at SG-20, and the fault-normal stress σ_{22} (Fig. S3e, bright green line) is accumulated, rather than released. This different stress behavior indicates that the patch around SG-0 is undergoing slip, yet in minor amount than the surrounding patches, whose additional release of normal stress is accumulated short distances away by frictionally stronger patches (i.e., SG-0), which undergo less accelerated slip. The negative fault-parallel stress variation σ_{11} (Fig. S3h, bright cyan line) indicates that the accelerated slip is inducing a compressive lobe through SG-0 (4, 5). This suggests that the accelerated slip is nucleating somewhere in the negative x_1-direction with respect to SG-0, and its rightward tip (view of Fig. 2a) swipes across the SG-0 station as it propagates in the positive x_1-direction. This 'tip' does not reach the SG-20 location, which does not measure any stress signal.

After the dynamic rupture initiates (Fig. S3c, f, and i), the anti-symmetric rupture pattern results in nearly constant, mildly compressive, fault-normal stress σ_{22} (after initial tensile and compressive peaks around 10 µs, Fig. S3f, dark green line). The fault-parallel stress σ_{11} experiences a fault-parallel compressive lobe σ_{11} at the SG-20 station (Fig. S3i, dark cyan line), consistent with the rupture propagating rightward (view of Fig. 2a). Note that the variations in the fault-parallel stress tend to leave a more persistent change in this case, while in the rapid pressure ramp-up case the fault-parallel stress changes have a more transient nature.

Materials and Methods

Specimen Configuration and Fluid-Injection Setup. In order to investigate the effects of fluids on the frictional faulting, a new hydraulic setup has been developed to inject pressurized water onto the interface of a Poly(Methyl Meth-Acrylate) (PMMA)

Table S1. Results from repeated fluid-injection experiments. Slow and fast nucleation have been performed on the same specimens under analogous nominal conditions. The first two tests are the ones presented in the manuscript. Couples of tests grouped between horizontal lines are conducted on the same specimen using the two fluid injection procedures – slow and fast, respectively – for direct comparison. To ensure consistent surface conditions, the interface is prepared before each test using the same procedures, including the polishing and bead-blasting procedure described in Materials and Methods. The "pressure" column gives the injected pore fluid pressure at the initiation of dynamic slip.

Angle (°)	Load (MPa)	Injection Rate	Pressure (MPa)
29	15.0	Slow	8.7
29	15.0	Fast	4.9
29	15.0	Slow	13.3
29	15.0	Fast	5.0
29	15.0	Slow	8.7
29	15.0	Fast	4.3
26	15.0	Slow	12.2
26	15.0	Fast	5.3

specimen (Figs. 1, 2, and S1). The specimen is a $200 \times 250 \times 12.5$ mm^3 PMMA prism divided into two identical halves by an oblique cut at an angle α with respect to the 200-mm dimension (Fig. 2). The juxtaposition of these two halves creates an interface (green-shaded area), whose surfaces have been polished and bead-blasted to obtain desired and repeatable tribological conditions (4). The micro-bead blasting procedure is performed via abrasive glass spherical particles between 104 and 211 µm in diameter. A thin duct is manufactured on the lower half of the specimen to allow the injection of pressurized fluid on the interface. Its diameter varies for machining purposes and equals 1 mm in the final 2.5-cm-long portion towards the interface (Figs. 2 and S1b, blue channel). The specimen assembly is compressed by a static pre-load P. In the experiments presented here we consider the specimen configuration with $P = 15$ MPa and $\alpha = 29°$. Upon the application of the external load P, the interface experiences a resolved normal and shear stress of $\sigma_{\mathrm{n}} = P\cos^2(\alpha) \approx 11.5$ MPa and $\tau_0 = P\sin(\alpha)\cos(\alpha) \approx 6.4$ MPa, respectively. Note that the load P is kept constant by setting the loading frame to switch to load-control mode after load has reached 15 MPa.

Under these constant-load conditions, the fluid is introduced onto the interface through the 1-mm-diameter duct by pressurizing it (Figs. 2 and S1a, blue channel), following either Procedure (1) or Procedure (2). As described in the main text, these procedures are characterized by a slow (5.3×10^{-3} MPa/s) or a fast (3.1×10^{1} MPa/s) pressure increase, respectively. The same specimen where Procedure (1) followed is subsequently used to conduct a test with Procedure (2). Yet, to guarantee consistent surface roughness, before each test the interface is prepared using the polishing and bead-blasting procedure described above. A list of four sets of tests – featuring slow and fast injection – is presented in Table S1. A new specimen is used for each pair of tests shown in the table.

A Buna-N rubber o-ring, placed at the bottom of the specimen, guarantees the seal from water spills; however, it adds a small thickness that is reduced as the specimen is compressed by the loading frame. This reduction in volume tends to squeeze a small quantity of fluid out onto the interface. For this reason, a 1-cm-long layer of (compressible) air, approximately corresponding to 3.1×10^{-8} m^3, is left on top of the fluid meniscus prior to starting the loading phase. After the desired far-field load is reached and the absence of liquid on the interface is confirmed, the fluid pressurization phase can begin.

The fluid-injection setup features an air-driven hydraulic pump connected to the specimen via a 2-m-long stainless-steel pipe (Figs. 1 and S1a), where a series of components are installed in order to achieve a wide range of water peak pressure (from $p_{\mathrm{amb}} \approx 0.1$ MPa to $p_{\max} \approx 17$ MPa), pressure rise-time (from 10^{-2} to 10^{1} MPa/s), and duration of pressure plateau. After being pressurized by the pump, the water pressure is modulated by a manual regulator (Figs. 1 and S1a). The pressure regulator allows a wide range of rising times, spanning from few MPa per hour (Fig. 3a) to few MPa per second. A solenoid valve, characterized by a rapid opening time, is employed to produce sharper rising times of the order of few MPa per tens of milliseconds (Fig. 3b), which would otherwise be impossible to replicate with the manual pressure regulator. In a zero-time-to-open approximation, the valve mimics a theoretical diaphragm separating a fluid at different pressure levels on either side. The sudden disappearance (opening) of such diaphragm gives rise to a Riemann problem (6, 7) in which a shock wave travels downstream of the pipe followed by a (slower) contact discontinuity, while an expansion fan travels upstream. The solenoid valve, which is actuated via a small electrical circuit, allows the creation of much sharper pressure ramp-up signals to be delivered to the specimen's interface (Figs. 2b and S1a). Two pressure transducers are located on either side of the solenoid valve in order to simultaneously measure the pressure upstream and downstream of it, regardless of the open or close configuration of the valve. These transducers are characterized by a cut-off frequency of 5 Hz and 3 kHz, respectively. For the sake of clarity, the same color scheme associated with each of the two pressure transducers in Figure S1a will be consistently adopted in the plots throughout the manuscript: purple refers to the pressure measured upstream of the solenoid valve and blue to the pressure downstream of it. The pressure value measured downstream of the valve is delivered to the specimen's interface (Fig. S1a). At ambient pressure and temperature, the speed of sound in water is approximately 1.5 km/s. In order to achieve pressure equilibrium over a 2-meter-long pipe, 5 ms are needed for 3 to 4 wave reverberations to occur. Considering that the shortest time scale in the injection circuit is that of the opening of the solenoid valve, which is in the order of tens of milliseconds, assuming pressure equilibrium between the pressure transducer downstream of the valve and the injection location on the specimen's interface is an acceptable approximation.

Local Pressure Measurements with the Tactile Sensor Film. The pressure transducers offer a high-resolved measurement of the pressure temporal evolution in the duct; however, they cannot quantify the pressure at other locations on the interface as the pressure diffuses away from the duct. For this reason, a separate experiment is conducted, where an array of holes of 0.5 mm in both diameter and depth is drilled over the bottom half interface of a specimen with an horizontal interface ($\alpha = 0°$) (Fig. 4a). Upon the juxtaposition of the two halves of the specimen, in correspondence to each hole, there is no surface contact and a small volume of air at ambient pressure ($p_{\mathrm{amb}} \approx 0.1$ MPa) is trapped there.

A 0.5-mm-thick tactile pressure-indicating sensor film characterized by a measurement range between 2.4 and 9.7 MPa (Fujifilm Prescale®) is inserted onto this interface before the two halves of the specimen are juxtaposed and loaded. The horizontal angle prevents slip during fluid-injection and preserves the integrity of the pressure film. The specimen is loaded at the same level of far-field normal stress experienced by a specimen with $\alpha = 29°$ and $P = 15$ MPa, i.e., $P|_{\alpha=0°} = 15\cos^2(29°) = 11.5$ MPa. When the final far-field load is applied to the specimen, the film experiences the resolved normal stress everywhere but in correspondence to the drilled holes, where no stress variation is recorded. The film locally and irreversibly changes color in proportion to the amount of pressure it experiences, with a spatial resolution is of 15 µm and an accuracy of ±2% (data provided by the manufacturer – Sensor Products Inc.)

Under these conditions, pressurized fluid is injected over the interface following a pressure profile equivalent to that of a slow pressure ramp-up scenario (Fig. 3a). As the fluid diffuses over the interface and fills the holes, the film coloration *within* each hole permanently changes whenever 2.4 MPa of pressure are exceeded (in Fig. 4c, the measured values of pressure smaller than 2.4 MPa have been manually set to the ambient pressure p_{amb}).

As the pore-pressure is increased, the water diffuses away from the injection location, driven by the pressure gradient, it fills the holes and it increases the pressure level inside them. This pressure increase induces *local* coloration in the film in proportion to the local-hole pressure level inside the holes. After the experiment is completed and the pressure film has assumed its final coloration, the chromatic levels are digitized by a digital camera and each pixel reading is then converted into a pressure level by using a calibration chart provided by the manufacturer (Sensor Products Inc.) and a map of pressure distribution along the interface is produced (Fig. 4b and c). Due to the pixel-to-pixel chromatic variation, for each hole, the pressure is computed as the average of the five smallest values therein: the less colored portions of each hole are typically located to its center and behold a more accurate pressure reading, as they are minimally affected by small irregularities associated with the interaction of the pressure film with the circular border of the hole.

In summary, the pressure measured by the film in correspondence to the population of holes is representative of the spatial distribution of pressure over the interface just prior the onset of the dynamic rupture (Fig. 4c).

Strain Acquisition System. On the back side of the specimen (Fig. 2b), two strain gauges are placed just below the interface (Fig. S1b): one in proximity to the injection location (namely SG-0) and the other 20 mm away from it (namely SG-20) in the positive x_1-direction. The strain gauges are connected to a digital acquisition system (Dewetron, Inc. DEWE-30-32) capable of collecting data over several minutes (at a reduced sampling rate) – during the nucleation phase (Fig. 7a and c; Figs. S2 and S3, a-b, d-e, g-h) – and also resolving the microsecond time scale once a triggering signal is received – for the dynamic rupture (Fig. 7b and d; Figs. S2 and S3, c, f, i). Using this technique, strain signals are acquired at temporal scales spanning over nine orders of magnitude (from 10^{-6} to 10^{3} s).

At the strain gauges locations, the stresses are computed from the measured strains by invoking linear-elastic constitutive properties in the plane-stress approximation ($\sigma_{33} = 0$). Since PMMA displays strain-rate dependent behavior (1, 8, 9) and our ruptures produce high strain rates (in excess of 10^{3} s^{-1} in correspondence to the rupture tip (1)), we have employed dynamic elastic modulus $E_{\mathrm{d}} = 5.9$ GPa (using the HSR wave speed values from Gori et al. (1)) to compute stress changes during the dynamic rupture, and the quasi-static elastic modulus $E_{\mathrm{qs}} = 2.4$ GPa (using the LSR wave speed values from Gori et al. (1)) for the nucleation phase, prior to the dynamic rupture (2, 3). Adjacent to the SG-0 station and across the interface from it, a retro-reflective tape is used to mirror the laser beam from a Polytec fiber-optic laser interferometer (model OFV-551) and provide the triggering signal for the 10-MHz sampling acquisition rate for the strain gauges as soon as the initiation of the dynamic event is detected.

Full-field Imaging with Digital Image Correlation. On the front side of the specimen (Fig. 2a) we employ the ultrahigh-speed digital image correlation (DIC) technique (10–12). A thin layer of white paint is deposited over the specimen lateral face and a 18×11 mm^2 random speckle pattern of optimally-sized black dots is added on top of it, centered at about 120 mm away from the injection location so that well-developed dynamic ruptures are captured as they swipe through it (1, 10, 11) (Fig. 2a). Digital images are acquired via a 400×250 pixel^2 Shumadzu HPV-X at 2 million frames per second, with the long dimension of the camera frame aligned with the inclined interface, in the x_1 and x_2-directions (Fig. 2a). The images are subsequently analyzed with the correlation software VIC-2D (Correlated Solutions Inc.) to produce full-field displacement evolution maps. In analogy with the strain acquisition system, the triggering signal is delivered by a laser velocimeter pointed at a retro-reflective tape placed just above the injection epicenter (Fig. S1b). The displacement fields are then filtered using a non-local (NL) de-noising algorithms (13, 14) and numerically differentiated with respect to time in order to obtain velocity fields and with respect to space to obtain strain fields. Stress maps are obtained from the strain ones by using linear-elastic constitutive properties of PMMA and, in particular, the dynamic value of the elastic modulus $E_{\mathrm{d}} = 5.9$ GPa.

Note that ultrahigh-speed DIC and strain gauges cannot be employed simultaneously in our experiments, as the high-power flash illumination required for the ultrahigh-speed image acquisition (15), releases a strong electro-magnetic pulse that interferes with the strain gauges compromising their ability to measure physical strains. The data has been acquired on nominally identical experiments.

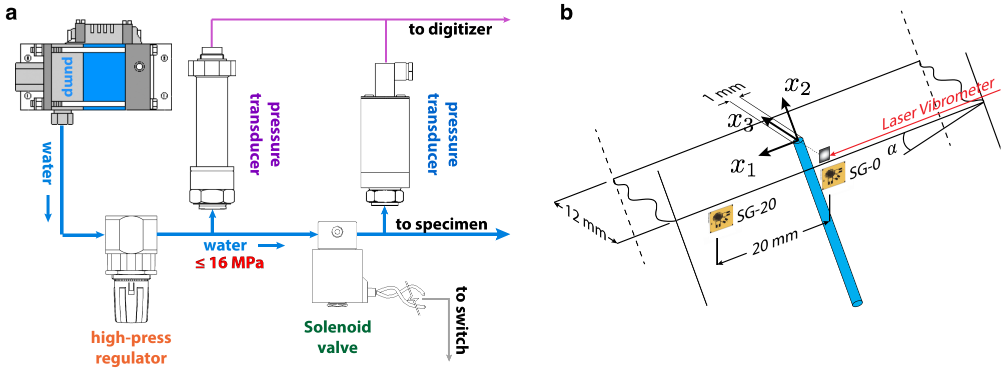

Fig. S1. **(a)** Schematic of the fluid-injection setup. A pump pressurizes water from ambient pressure ($p_{\mathrm{amb}} \approx 0.1$ MPa) up to 17 MPa. Downstream of the pump, the pressurized water flows through a series of components: (**i**) a high-pressure regulator for manual pressure modulation (from few MPa/min to few MPa/s); (**ii**) a pressure transducer with a 5 Hz bandwidth; (**iii**) a solenoid valve, allowing sharp pressure ramp-up profiles (in the order of few tens of MPa/s); and (**iv**) a pressure transducers with bandwidth of 3 kHz measuring the fluid pressure just upstream of the specimen. Note that the two pressure transducers are placed on either side of the solenoid valve. **(b)** Close-up view of the frictional interface of the specimen around the injection location. The two strain gauges are glued on the back side (Fig. 2b). The laser vibrometer signal is used to detect sudden motion in the x_1-direction associated with the dynamic rupture event and trigger the acquisition of the strain signals at high-bandwidth (1 MHz).

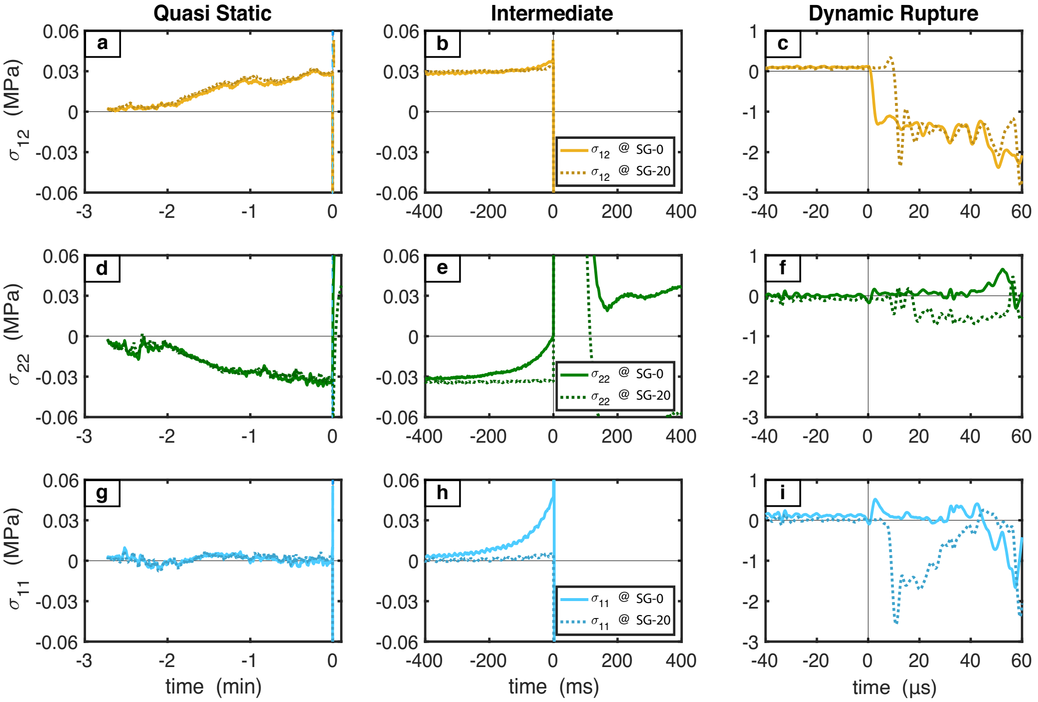

Fig. S2. Temporal evolution of the shear **(a-c)**, fault-normal **(d-f)** and fault-parallel **(g-i)** stresses recorded by the two strain-gauge stations (Figs. 2b and S1b) during the rapid pressure ramp-up over three time scales: minutes **(a)**, **(d)** and **(g)**, milliseconds **(b)**, **(e)** and **(h)**, and microseconds **(c)**, **(f)** and **(i)**. Time $t = 0$ indicates rupture initiation. Prior to the valve opening **(a)**, **(d)** and **(g)**, no fluid has been delivered to the interface yet, and stresses accumulate as a consequence of the viscoelastic relaxation of the bulk polymer under constant external load. After the valve opening, in the few hundred of milliseconds prior to the rupture initiation, the stress minimally redistributes due to the limited accelerated slip precursoring the incipient dynamic event. After the rupture is triggered **(c)**, **(f)** and **(i)**, a (left-lateral) dynamic slip event is recorded.

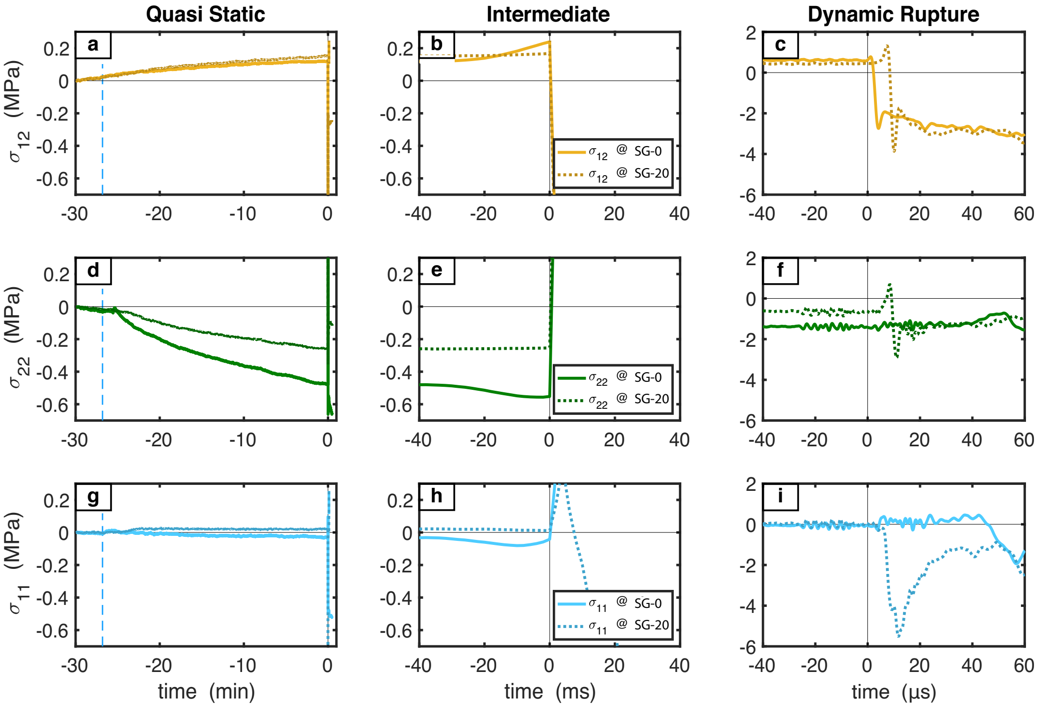

Fig. S3. Temporal evolution of the shear **(a-c)**, fault-normal **(d-f)** and fault-parallel **(g-i)** stresses recorded by the two strain-gauge stations (Figs. 2b and S1b) during the gradual pressure ramp-up over three time scales: minutes **(a)**, **(d)** and **(g)**, milliseconds **(b)**, **(e)** and **(h)**, and microseconds **(c)**, **(f)** and **(i)**. Time $t = 0$ indicates rupture initiation. The delivery of pressurized fluid begins approximately 27 minutes prior to the rupture initiation **(a)**, **(d)** and **(g)** (water droplet symbol), promoting slow slip. Note that stresses partially accumulate as a consequence of the viscoelastic relaxation of the bulk polymer under constant external load. In the few tens of milliseconds loading to the rupture initiation, the stress redistributes due to the local accelerated slip at SG-0 precursoring the incipient dynamic event. After the rupture is triggered **(c)**, **(f)** and **(i)**, the fault-parallel and shear-stress drops are about twice as large as the rapid-ramp up counterparts (Fig. S2).

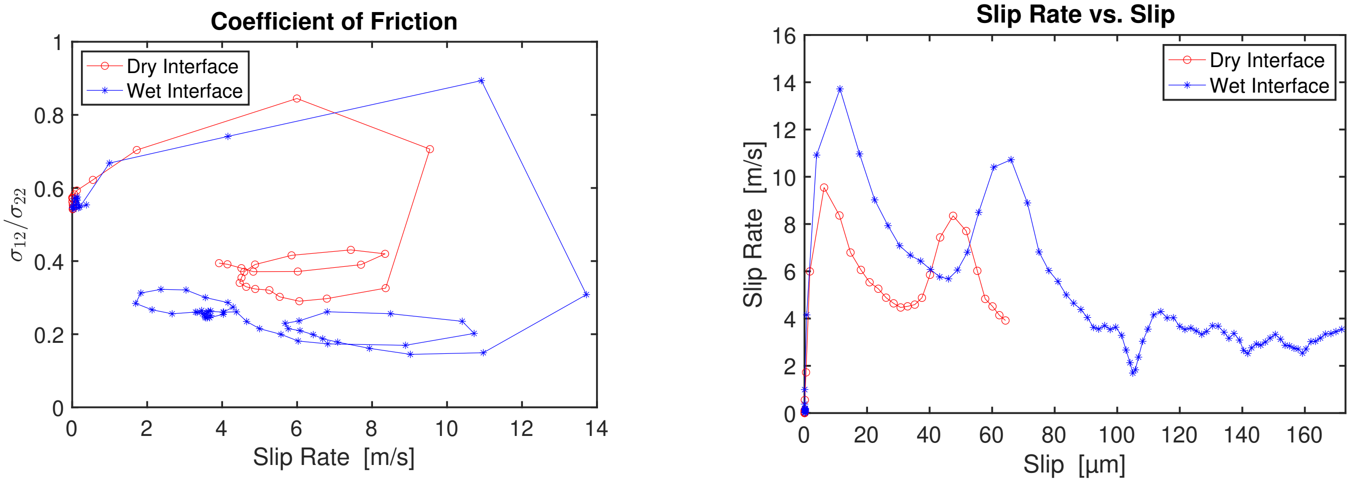

Fig. S4. Evolution of friction with slip rate (**left**) and evolution of slip rate with slip (**right**) along a dry (red) and pre-wetted (blue) interface. Friction is obtained as the ratio of shear to normal stress. Stresses, slip and slip rate are measured using the ultrahigh-speed digital image correlation method over a field of view of size 18×11 mm^2. The curves are obtained for a point at the center of the field of view, with other locations showing similar behavior. The two tests are conducted under the same nominal loading conditions of $P = 15$ MPa and $\alpha = 29^\circ$. In these tests, ruptures are initiated using a different procedure, not involving fluid-injection (as described in the text), so as to better characterize the role of pre-existing fluids on the interface.

References

1. M Gori, V Rubino, AJ Rosakis, N Lapusta, Pressure shock fronts formed by ultra-fast shear cracks in viscoelastic materials. *Nat. Commun.* **9**, 4754 (2018).
2. I Svetlizky, E Bayart, G Cohen, J Fineberg, Frictional resistance within the wake of frictional rupture fronts. *Phys. Rev. Lett.* **118**, 234301 (2017).
3. E Bayart, I Svetlizky, J Fineberg, Slippery but Tough: The Rapid Fracture of Lubricated Frictional Interfaces. *Phys. Rev. Lett.* **116**, 194301 (2016).
4. M Mello, HS Bhat, AJ Rosakis, H Kanamori, Identifying the unique ground motion signatures of supershear earthquakes: Theory and experiments. *Tectonophysics* **493**, 297–326 (2010).
5. M Mello, HS Bhat, AJ Rosakis, Spatiotemporal properties of Sub-Rayleigh and supershear rupture velocity fields: Theory and experiments. *J. Mech. Phys. Solids* **93**, 153–181 (2016).
6. HW Liepmann, A Roshko, *Elements of gasdynamics.* (Courier Corporation), (1957).
7. PL Roe, Approximate Riemann solvers, parameter vectors, and difference schemes. *J. computational physics* **43**, 357–372 (1981).
8. H Lu, X Zhang, WG Knauss, Uniaxial, shear, and Poisson relaxation and their conversion to bulk relaxation: studies on poly (methyl methacrylate). *Polym. Eng. & Sci.* **37**, 1053–1064 (1997).
9. CR Siviour, JL Jordan, High strain rate mechanics of polymers: a review. *J. Dyn. Behav. Mater.* **2**, 15–32 (2016).
10. V Rubino, AJ Rosakis, N Lapusta, Full-field Ultrahigh-speed Quantification of Dynamic Shear Ruptures Using Digital Image Correlation. *Exp. Mech.* **59**, 551–582 (2019).
11. V Rubino, AJ Rosakis, N Lapusta, Understanding dynamic friction through spontaneously evolving laboratory earthquakes. *Nat. Commun.* **8** (2017).
12. MA Sutton, JJ Orteu, H Schreier, *Image correlation for shape, motion and deformation measurements: basic concepts, theory and applications.* (Springer Science & Business Media), (2009).
13. A Buades, B Coll, JM Morel, Nonlocal image and movie denoising. *Int. J. Comput. Vis.* **76**, 123–139 (2008).
14. V Rubino, N Lapusta, AJ Rosakis, S Leprince, JP Avouac, Static laboratory earthquake measurements with the digital image correlation method. *Exp. Mech.* **55**, 77–94 (2015).
15. HZ Xing, QB Zhang, CH Braithwaite, B Pan, J Zhao, High-Speed Photography and Digital Optical Measurement Techniques for Geomaterials: Fundamentals and Applications. *Rock Mech. Rock Eng.* **50**, 1611–1659 (2017).